Advances in Materials Technology for Fossil Power Plants
Proceedings from the Eighth International Conference
October 11–14, 2016, Albufeira, Algarve, Portugal
https://doi.org/10.31399/asm.cp.am-epri-2016p0888

J. Parker, J. Shingledecker, J. Siefert, editors

CORROSION OF NICKEL-BASE ALLOYS BY SUPERCRITICAL CO2

R.I Olivares and W. Stein
CSIRO Energy Centre, 10 Murray Dwyer Circuit, Steel River Estate, Newcastle, Australia

T.D. Nguyen and D.J. Young
School of Materials Science & Engineering, University of New South Wales, Sydney, Australia

ABSTRACT

Nickel-base alloys were exposed to flowing supercritical CO_2 (P = 20MPa) at temperatures of 700 to 1000°C for up to 1000 h. For comparison, 316L stainless steel was similarly exposed at 650°C. To simulate likely service conditions, tubular samples of each alloy were internally pressurised by flowing CO_2, inducing hoop stresses up to 35 MPa in the tube walls. Materials tested were Haynes alloys 188, 230 and 282, plus HR120 and HR160. These alloys developed chromia scales and, to different extents, an internal oxidation zone. In addition, chromium-rich carbides precipitated within the alloys. Air aging experiments enabled a distinction between carburisation reactions and carbide precipitation as a result of alloy equilibration. The stainless steel was much less resistant to CO_2 attack, rapidly entering breakaway corrosion, developing an external iron-rich oxide scale and internal carburisation. Results are discussed with reference to alloy chromium diffusion and carbon permeation of oxide scales.

Keywords: supercritical, carbon dioxide, oxidation, carburisation, chromia scales, diffusion.

INTRODUCTION

Supercritical CO_2 (SCO_2) has advantages as a heat transfer medium and as the working fluid in a closed Brayton cycle turbine [1]. For these reasons it is being investigated for use in concentrated solar thermal power generation [2] and in Generation IV Fast Nuclear Reactors [3]. However, hot CO_2 can be highly corrosive.

Atmospheric pressure CO_2 causes internal carburisation as well as external oxide scaling on stainless steel and Fe-Cr alloys [4-9], Fe-Ni-Cr alloys [10,11], and ferritic-martensitic Fe-9Cr steels [13,14]. Pressurised CO_2 (10 – 20 atm) causes the same form of corrosion on low alloy steels [12]. Autoclave experiments with SCO_2 [15-17] have also produced internal carburisation and external oxide scaling of low alloy steels, P91 steel and a variety of chromia-forming, heat resisting alloys.

The gas reactions

$$CO_2 = CO + ½O_2 \quad (1)$$
$$2CO = CO_2 + C \quad (2)$$

lead to very low carbon activity, a_C, values in pure CO_2, and the gas itself is clearly not carburising. However, reacting alloys are in contact with the undersides of oxide scales, where conditions are quite different. The value of a_C is controlled by the equilibrium of reactions (1) and (2) with a low pO_2 value set by the metal-metal oxide local equilibrium. It has been calculated [18] that the maximum value of a_C beneath a scale of $FeO+FeCr_2O_4$ exposed at 650°C to pCO_2 = 0.2 atm is 0.52. Examination of an Fe-9Cr alloy exposed to these conditions showed that the volume fraction of internal carbide was in agreement with thermodynamic prediction. Furthermore, the measured rate of carburisation was as predicted from Wagner's theory of internal corrosion [19], for a carbon permeability corresponding to a_C = 0.25. Evidently, local equilibrium is very closely approached in this case.

Supercritical CO_2 has the potential to generate very high a_C values. However, this occurs only if carbon can pass through the oxide scale. Alloys designed for use at intermediate temperature develop chromium-rich oxide scales, usually Cr_2O_3, in which carbon is known [20] to be insoluble. Nonetheless, carbon is in some cases transmitted through these scales, a process now known [21] to occur via oxide grain boundaries.

Whether or not carbon passes through chromia scales is known to vary with alloy chromium level [18], whether the alloy is iron or nickel base [23] and the presence of reactive gas phase impurities [24]. It seems likely that the stress state of the oxide would also be important. Earlier work on corrosion in SCO_2 was carried out in autoclaves [15-17]. Whilst this approach provides realistic fluid pressures and temperature, it subjects alloy specimens and their oxide scales to isostatic compression. This stress state does not reflect service conditions, under which SCO_2 flows through tubing, inducing hoop stresses in the tube wall.

The aim of this paper was to investigate the corrosion resistance of Ni-base alloys to supercritical CO_2 under realistic stress conditions, and to compare the results with those of lower Ni content alloys.

.

EXPERIMENTAL

High temperature nickel alloys with the mill certificate compositions given in Table 1, were supplied by Haynes International in the form of a solid rods, 1 m in length and 25 mm in diameter. Gun drilling along the centre was used to fabricate a tube of 6 mm internal diameter with wall thickness of 9.5 mm. The full length of the rod was drilled in one direction, producing an inner bore with eccentricity within ±1 mm and a surface finish of ≤ 3.4 μm. Both ends of the tube were threaded to connect high pressure fittings (Autoclave Engineers) for attachment of CO_2 supply and exit lines. In the case of 316 stainless, commercially available tubing with nominal dimensions of 6.35 mm outside diameter and 2.11 mm inside diameter was used. In each case, the whole tube was the test specimen, and it was mounted via an alumina sleeve inside a horizontally split tube furnace of three independently controlled heating zones. Heating zones were adjusted such that the middle of the tube inside the furnace achieved a maximum temperature of 1000°C and the temperature gradually dropped to 400°C at the two furnace ends. The length of the tube furnace was 600 mm, and the portion of the tube at the centre of the furnace exposed to the profile 700-1000-700°C, was a total of 500 mm. Outer surface temperatures of the tube specimen were monitored at all times using thermocouples. The atmosphere in the furnace, which contacted the tube outer surface was laboratory air.

Table 1. Alloy composition analyses (wt%).

Alloy	Ni	Cr	Co	Mo	Ti	Al	Fe	Mn	Si
Haynes 282	bal	19.4	10.2	8.5	2.2	1.38	0.4	0.03	0.05
Haynes 188[a]	23.0	22.2	bal	--	--	--	2.6	0.85	0.25
HR120	37.3	24.8	0.1	0.2	<0.01	0.05	bal	0.69	0.52
HR160	bal	27.8	30.1	0.1	0.55	--	0.3	0.47	2.58
Haynes 230[b]	bal	21.7	0.1	1.4	< 0.01	0.44	2.0	0.50	0.44
316L	11.23	17.0	--	2.1	--	--	bal	1.66	0.40

[a] Contains 14.3 W [b] Contains 14.2 W

Supercritical CO_2 at 20 MPa (SCO_2) was generated from high grade liquid CO_2 supply cylinder via an SFT-10 Carbon Dioxide Pump. The liquid CO_2 analysis certificate showed 99.99 vol% CO_2, 2 ±1ppm O_2 and 5 ±2ppm H_2O. Flowing SCO_2 at 20 MPa pressure was maintained by controlling the exit mass flow at an average of 0.2 g/min and the experiment was continued uninterrupted for 1000 h. After this exposure, the tube was filled with a cold setting resin to protect its inner surface during subsequent handling. Sample rings of 5 mm width were cut from four different tube locations corresponding to the exposure temperatures of 700, 800, 900 and 1000°C. The temperature variation along the 5 mm tube sections was 20°C for the nominal temperature of 700°C, 12°C for the nominal temperature of 800°C, 6°C for the nominal temperature of 900°C, and 2°C for the nominal temperature of 1000°C. Polished cross-sections of the reacted samples were examined by scanning electron microscopy (SEM) using energy dispersive spectrometry (EDS). These sections were subsequently etched with a solution of 10 ml glycerine + 6 ml HCl and 3 ml HNO_3, to reveal carbide precipitates.

.

RESULTS

Oxidation of High Nickel Alloys

Typical cross-sections of the high nickel alloy tube wall inner surfaces after contact with SCO_2 are shown in Fig. 1. Exposure times were 1000 h in all cases except for Haynes 282, for which the experiment terminated after 658 h. In all cases, an external scale was found, along with a sub-surface zone of internal oxidation in all alloys except HR120.

Analysis by EDS revealed that the external scale was made up principally of a dense, almost pure chromia layer. A thinner layer of $MnCr_2O_4$ developed at the scale-gas interface for Haynes 230 and Haynes 188 The spinel layer became a larger fraction of the total scale thickness at higher temperatures, and was not detected after reaction at 700°C.

A silica sublayer developed at the scale-alloy interface to different extents on the various alloys. On HR160, a continuous layer of silica developed, becoming thicker at higher temperatures. On HR120, the silica layer was extensive, but not quite continuous. In the case of Haynes 188, silica formed as isolated islands at the chromia-alloy interface. No silica was found at the scale-alloy interface for Haynes 230 or Haynes 282. In the latter alloy, a discontinuous Ti-rich inner oxide layer was developed instead. Chromia spallation was extensive on HR160 after cooling from 1000°C. Total scale thicknesses (spinel+Cr_2O_3+SiO_2) developed in 1000 h of reaction at the different temperatures are compared for the high nickel alloys in Figure 2(a). Thickness values for alloy Haynes 282 were calculated from measurements made after 658 h on the assumption

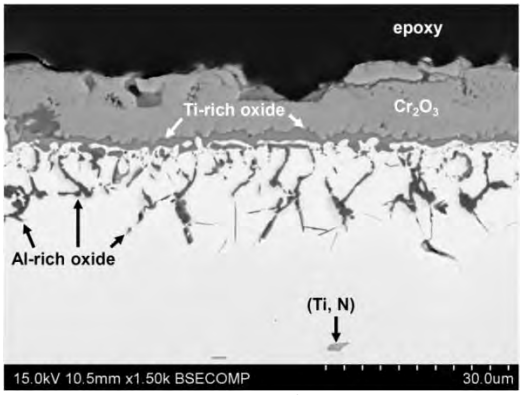

(a) Haynes 282, 900 °C, 658 h

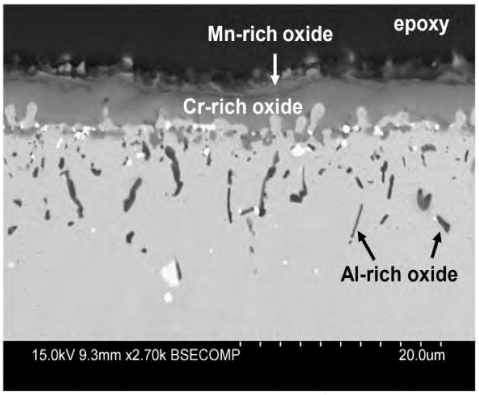

(b) Haynes 230, 900 °C, 1000 h

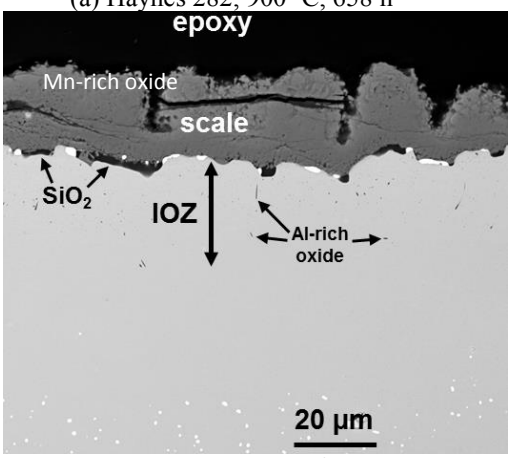

(c) Haynes 188, 1000 °C, 1000 h

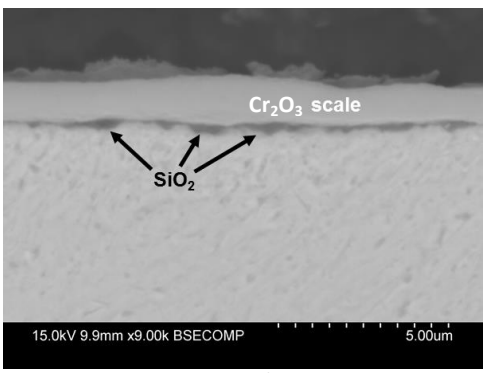

(d) HR120, 700 °C, 1000 h

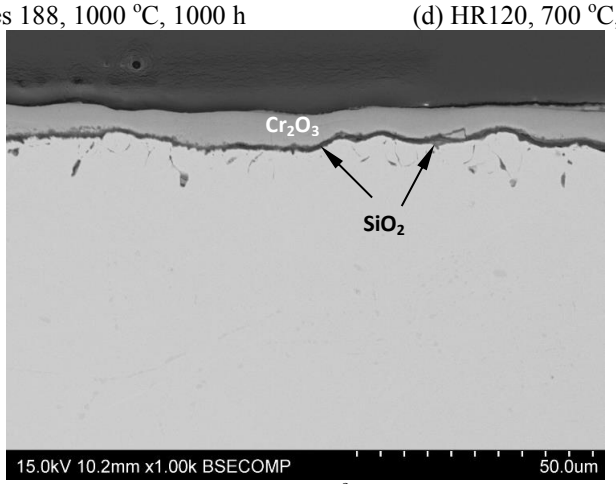

(e) HR160, 800 °C, 1000 h

Figure 1 Cross-sections of high Ni alloys after exposure to flowing SCO_2.

that scaling kinetics were parabolic

$$X^2 = 2k_p t \tag{3}$$

with X the total scale thickness formed in time, t, and k_p the parabolic rate constant.

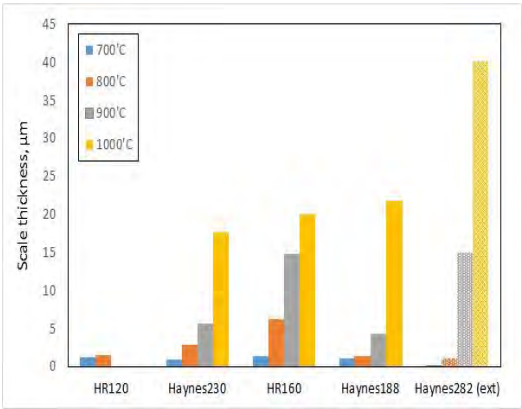

(a) Scale thickness

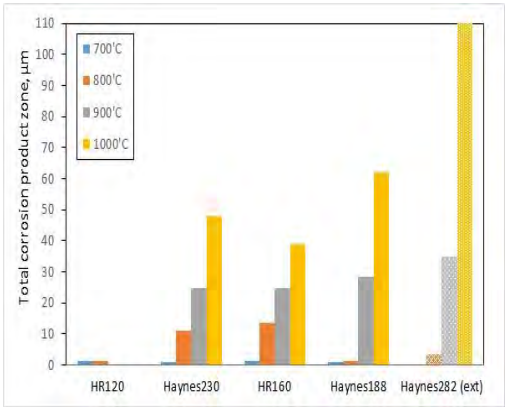

(b) Scale plus internal oxidation zone

Figure 2 Oxide corrosion products developed in 1000 h reaction with SCO_2 at 20 MPa, with data for Haynes 282 extrapolated from 658 h (see text).

Internal oxides developed in all the high nickel alloys were found by EDS to be Al-rich. Additional bright contrast precipitates visible in Figures 1 (b) and (c) are tungsten-rich carbides which were present in the original alloys. These oxide precipitates were large, and somewhat elongated in a direction normal to the alloy surface. In addition, very fine, spheroidal precipitates were observed immediately beneath the surface of Haynes 230. These were too small for EDS analysis, but could have been silica.

Internal oxidation zone depth varied among the alloys, and increased with temperature. An approximate measure of scale damage is provided by the sum of scale thickness and internal oxidation depth, shown for the different alloys as a function of temperature in Figure 2(b). Although temperature sensitivities are substantial, oxidation rates are seen not to be excessive in the range of practical interest.

Carbide Precipitation in High Nickel Alloys

Carburization is potentially a threat to these alloys, because, should it occur, the process is so rapid [24]. All reacted specimens were examined for carbides by etching metallographic cross-sections. Typical results are shown in Figure 3, where carbide precipitates are visible as grey coloured particles. The general pattern of precipitation was the same in all alloys. A carbide free zone developed in the alloy sub-surface region, but carbides appeared throughout the rest of the tube wall thickness. Precipitation occurred preferentially on alloy grain boundaries, and occurred uniformly through the tube wall.

To distinguish between carburization (by carbon uptake from the gas) and aging of the as received alloy microstructures, alloy samples were annealed at 1000°C for 1000 h under an atmosphere of laboratory air. This treatment produced carbide precipitates of the same size and locations, and at the same volume fraction level as did the same time of treatment in SCO_2 at this temperature. Clearly the carbide precipitates are the result of alloy microstructure aging, and do not reflect subsurface attack by carbon from the gas.

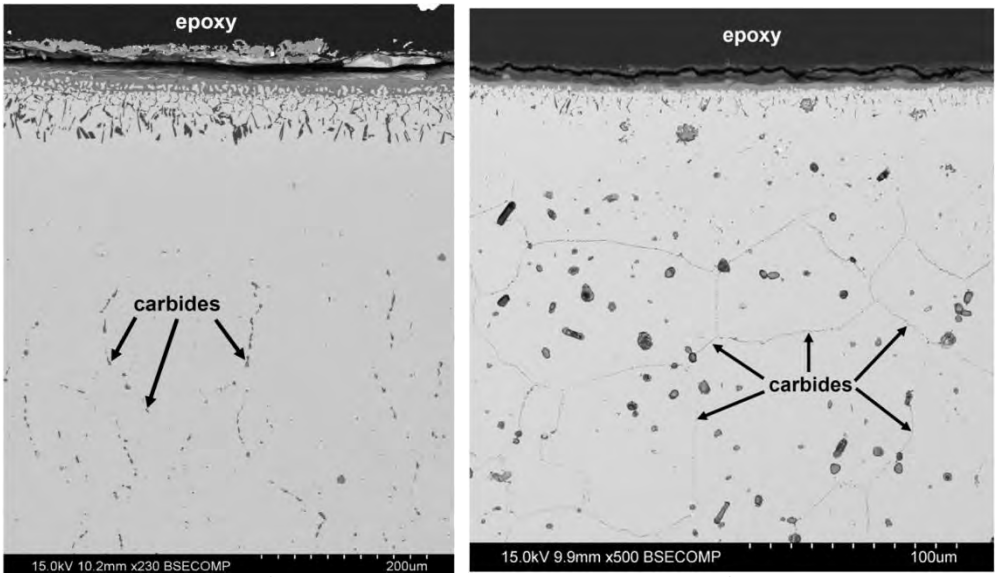

(a) Haynes 282, 1000 °C, 1000h (b) HR230, 900 °C, 1000h

Figure 3 Carbide precipitation within high nickel alloys reacted in SCO_2.

Corrosion of 316 Stainless Steel

The stainless steel was reacted with SCO_2 in the same way as the high nickel alloys, but at a maximum temperature of 650°C. Under these conditions it underwent both oxide scaling and internal carburization, as shown in Figure 4 [25]. The scale was not uniform: in some places, a thin scale formed, whereas in other locations substantially thicker nodules grew. Beneath the scale–alloy interface, local precipitates of varying size had developed in a narrow subsurface zone. Identified by EDS analysis as MnS, they result from sulphur rejection from the scale and the MnS solubility product being exceeded in the sulphur-enriched subsurface zone.

Analysis by EDS showed the thin scale regions seen in Figure 4(a) to consist of M_2O_3, iron-rich in its outer region and chromium-rich in its inner region. The nodules consisted of an outer layer of pure iron oxide and an inner region of composition approximating to $(Fe_xCr_{1-x})_3O_4$. These nodules both thickened and grew laterally with time, so that the surface area fraction covered by the more rapidly growing iron oxide increased. Clearly, the scale developed by the 316 stainless steel was nonprotective.

The precipitation pattern seen in Figure 4(b) reflects the formation of both intergranular and intragranular chromium-rich carbides. In order to determine if these carbides are a result of carbon ingress from the gas, or merely alloy aging, a sample of 316 was annealed in air at 650°C for 1000 h. Metallographic examination of the air-annealed 316 revealed the appearance of chromium-rich carbides, but restricted in the main to intergranular locations. Quantitative image analysis showed the volume fraction of carbides in the air annealed steel to be $f_V = 0.013$, compared with $f_V = 0.046$ after reaction in SCO_2 for the same time. Thus additional carbon uptake occurred during reaction with SCO_2.

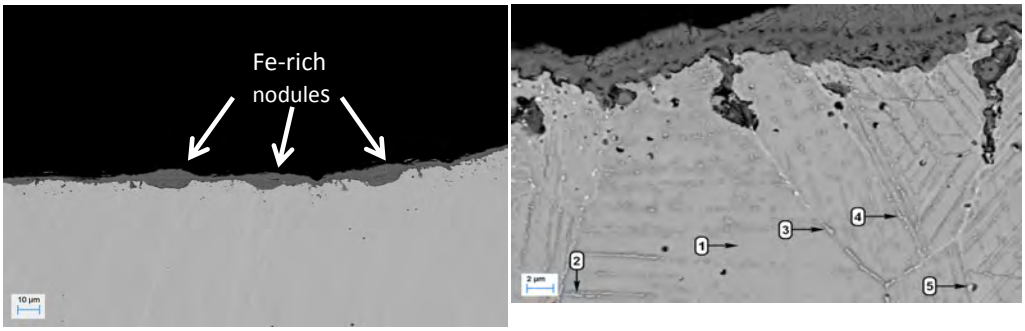

(a) Unetched (b) Etched to reveal carbides

Figure 4 Stainless steel 316 after exposure to SCO_2 at 650 ^oC [25].

DISCUSSION

High Nickel Alloys

All five alloys developed protective chromium-rich scales, which grew slowly and prevented carbon from the gas entering the underlying alloy. The disposition of reaction products is in all cases consistent with local equilibrium established in a gradient of oxygen activity from its maximum at the scale-gas interface to a minimum in the alloy interior. Thus the most stable oxide, alumina, forms as an internal precipitate; the next most stable product, silica, develops at or immediately beneath the scale-alloy interface; the less stable chromia makes up the majority of the scale and manganese spinel grows at the scale-gas interface.

Differences in scale microstructures reflect the different alloy compositions. Alloy HR160, with 2.6 Si (all compositions in wt.%), forms a continuous layer of silica, whereas HR120 with 0.5 Si develops a semi-continuous layer. The other alloys with lower Si levels form scattered silica islands at the chromia-alloy interface and/or internal precipitates. Haynes 282, with very little Si, but 2.2Ti develops a Ti-rich innermost oxide layer rather than silica. The very low Mn content of this alloy explains its failure to produce an outer spinel scale layer.

Internal oxidation in many cases affected greater depths of alloys than was consumed in growing their scales. Nonetheless, the extent of attack was not large. Assuming that inward penetration of the precipitation zone is diffusion controlled, then if Al diffusion is ignored, the kinetics are parabolic [26]

$$X_i^2 = 2k_p^{(i)}t \tag{4}$$

with

$$k_p^{(i)} = \frac{N_O^{(s)} D_O}{\nu N_{Al}} \tag{5}$$

Here X_i is the internal oxidation depth formed in time, t, $k_p^{(i)}$ the rate constant, $N_O^{(s)}$ the concentration of dissolved oxygen at the scale-alloy interface, D_O the diffusion coefficient for oxygen in the alloy matrix, N_{Al} the original alloy concentration of aluminium and ν the

stoichiometric coefficient for the precipitate compound AlO_v. For a given precipitate and temperature then, the rate of internal attack depends on alloy Al content and oxygen permeability. Of the three Ni-base alloys Haynes 282, 230 and HR160, alloy 282 has the highest value of N_{Al}, but also shows the highest rate of internal attack. Assuming D_O to be closely similar for the alloys, it follows that the dissolved oxygen content is higher beneath the scale formed on alloy 282.

The Ti-rich oxide layer formed at the chromia-alloy interface on 282 is discontinuous, and regions of chromia-alloy contact will produce an oxygen activity greater than that in effect at the silica-alloy interface formed by HR160. Since $N_O^{(s)}$ is proportional to oxygen activity, the relative internal oxidation rates of the two alloys is thereby accounted for. However, alloy 230 also develops a chromia-alloy interface, and would also on that basis be expected to undergo faster internal oxidation. A further difference between alloys 282 and 230 is the much lower level of manganese in the former. Incorporation of Mn into the chromia formed on alloy 230 would stabilize the oxide, lowering the scale-alloy local oxygen activity and slowing internal oxidation.

The overall extent of reaction for all high nickel alloys is small. If steady-state parabolic kinetics are in effect, then useful lifetimes can be expected. The apparent thermodynamic stability of the reaction product phase assemblages suggest that a steady state has in fact been achieved. Part of the reason for this is the absence of chromium volatilization. In the dry gas used here, volatile $CrO_2(OH)_2$ formation is impossible. Furthermore, at the low oxygen activities prevailing in pure CO_2 (p_{O_2} = 8 x 10^{-9} atm at 700°C and 2 x 10^{-6} atm at 1000°C), the reaction

$$Cr_2O_3 + \frac{3}{2}O_2 = 2CrO_3(g) \qquad (6)$$

is not favoured.

A further reason for the maintenance of a steady state in the CO_2 corrosion of the high Ni alloys is the avoidance of internal carburization. Carbon uptake from the gas, if it occurs, removes chromium from the alloy matrix as Cr-rich carbide, decreasing its ability to reform protective chromia when scale failure occurs. Discussion returns to this point after consideration of the 316 stainless steel failure.

316 Stainless

Examination of the oxide scale on 316 stainless shows that an initially protective Cr-rich oxide is progressively replaced by faster growing Fe-rich oxides. The same phenomenon is observed [16] in the static environment of an autoclave experiment, although at a slightly slower rate. The question of interest concerns the reason for failure of this steel in the SCO_2 reaction, in contrast to its successful passivation in air or oxygen.

Corrosion of 316 in SCO_2 led to the precipitation of 4.6 vol. % of chromium carbide in the subsurface region of the steel [25]. If the carbide is assumed to be $Cr_{23}C_6$, it can be calculated from the densities of the carbide and austenite that the corresponding amount of chromium removed from the steel matrix is 4 wt. %. Thus the initial chromium concentration is reduced from 17 to 13 wt. %. If the initial, protective Cr-rich scale is damaged, additional chromium for its repair is needed from the alloy. As carburization proceeds, less and less chromium is available for this purpose, and chromium oxide regrowth is prevented, allowing iron oxide nodule nucleation.

Comparison of the poor performance of 316 stainless with the successful corrosion resistance displayed by the high nickel alloys is made more complex by the higher chromium levels of the latter. This difficulty is avoided by using data available [25] for Hastelloy-C276 (Ni-17Cr-17Mo-9Fe-0.2Si-0.2Mn). Although the Ni-base alloy contains the same chromium level as 316 stainless, when exposed to SCO_2 under the same conditions, the Hastelloy maintained a protective chromia scale whereas the stainless steel failed to do so.

Given that the two austenitic alloys would have rather similar chromium diffusion coefficients, their ability to support continued growth of chromia scales is expected [19] also to be similar. However, whilst this chromium level was evidently sufficient for protective Cr_2O_3 scale formation on Hastelloy-C276, it proved inadequate for 316 stainless, resulting in nucleation and growth of Fe-rich oxide. The lower oxidation resistance of 316 is associated with carbide precipitation in the Fe–Cr based alloy at the SCO_2 pressures investigated. Once carbide precipitation became extensive in 316 stainless, the steel lost its ability to repassivate.

Alloy Carburisation Resistance

An alloy which does not carburise retains a higher level of matrix chromium available to sustain growth of a protective chromia scale, and to regrow that scale when damaged. This is a factor in the success of the high nickel alloys, all of which retained protective oxide scales and none of which underwent carburisation. It is therefore of interest to enquire into the intrinsic carburization resistance of both nickel and iron based materials.

The thermodynamics of carbide precipitation are modelled using the Fe-17Cr-C and Ni-17Cr-C systems. The reaction investigated is

$$23\underline{Cr} + 6\underline{C} = Cr_{23}C_6, \quad K_{sp} = N_{Cr}^{23} N_C^6 \tag{7}$$

where underlining indicates a solute species K_{sp} is the solubility product for the carbide and N denotes mol fraction. Dissolution of iron in the carbide is ignored. Using thermodynamic data from Kubaschewski et al. [27] for the free energy of carbide formation and partial molar enthalpies of Cr and C dissolution, one calculates the values at high temperature for K_{sp} shown in Table 2. Clearly, carbide formation is more favoured in the iron-base alloys.

Table 2 Carbide stabilities in model binary alloys

Alloy	K_{sp}	
	900°C	**1000°C**
γ-Fe-Cr	1×10^{-29}	4×10^{-27}
Ni-Cr	1×10^{-25}	8×10^{-24}

Calculation for 650°C leads to the values of K_{sp} shown in Table 3. Using values of N_{Cr} for the binary 17% alloys in Eq. (7) then leads to the minimum carbon concentrations, N_C^{min}, required for carbide formation and the corresponding a_C values shown in the Table. The results reflect the lower solubility of carbon in Ni, and the decreased stability of $Cr_{23}C_6$ with respect to Ni-Cr-C solid solution. To carburise the Ni-base alloy is seen to require a carbon activity value two orders of magnitude greater than is needed for the Fe-base alloy. At least in part, this explains the differing carburisation susceptibilities of the stainless steel and the Hastelloy, a conclusion which extends to the other high nickel alloys.

Table 3 Carbon activities required for carburisation of model Cr alloys

	Fe-17Cr	Ni-17Cr
K_{sp}	1.8 x 10^{-36}	3.6 x 10^{-33}
$N_C^{(min)}$	6.3 x 10^{-7}	5.2 x 10^{-6}
a_C	2.3 x 10^{-5}	3.2 x 10^{-3}

A further factor contributing to the greater carburization resistance Ni-base alloys, is the difference in their carbon permeability, $N_C D_C$. Whether or not an alloy forms a protective chromia scale depends on the relative rates at which alloy chromium diffuses out to the surface (to sustain selective Cr_2O_3 growth) and carbon permeates inwards to precipitate the chromium. As seen in Eq. (5) the rate of the latter process is proportional to $N_C D_C$.

Values of carbon solubility and diffusivity have been measured at high temperatures [28,29] for Fe-Ni binary alloys. To a good approximation, the alloy matrix remaining after chromium precipitation can be modelled on this binary system. Extrapolation from these results to a temperature of 650°C [30] yields the results shown for a value of $a_C = 1$ in Figure 5. As is seen,

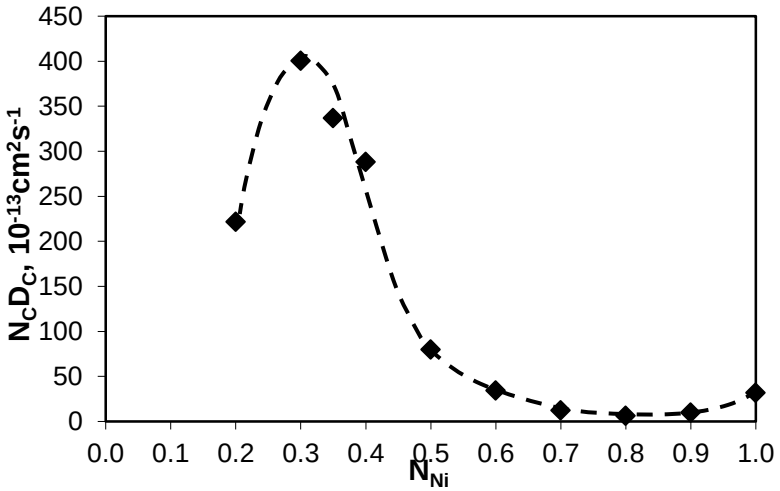

Figure 5 Carbon permeability in Fe-Ni alloys at 650 °C, extrapolated from high temperature data.

high nickel alloys have carbon permeabilities about two orders of magnitude lower than do stainless steel type compositions.

A final factor contributing to the superior performance of high nickel alloys is the nature of the oxide scales they develop. Chromia scales grow by grain boundary diffusion, and it has recently been shown [21] that carbon penetrates the scale via the same pathway. It is highly likely that the presence of other alloy constituents on the oxide grain boundaries affects their transport properties. The difference between chromia scales grown on iron and nickel base alloys has not yet been determined with respect to grain boundary segregation, although iron has been found [31] by atom probe tomography to be enriched at chromia grain boundaries in a scale grown on Fe-20Cr in atmospheric pressure CO_2.

CONCLUSIONS

Oxidation of five high nickel, chromia-forming alloys in SCO_2 leads to protective scale growth and some internal oxidation at temperatures of 700-1000^oC. In contrast, 316L stainless steel reacts at 650^oC to form iron-rich oxide nodules, which spread laterally to form a continuous, non-protective scale.

High nickel alloys show no sign of carbon uptake from the gas, but the stainless steel carburizes, precipitating internal chromium-rich carbides. This process removes about 4 wt. % Cr from the steel matrix, decreasing its ability to maintain exclusive chromia scale growth.

Reasons for the superior carburization resistance of the high nickel alloys are shown to include the lower thermodynamic stability of chromium carbide and lower carbon permeabilities in a nickel rich matrix. It is also possible that the chromia grown on a high nickel alloy has different grain boundary transport properties, and is therefore better able to resist carbon transmission from the gas to the substrate alloy.

ACKNOWLEDGEMENT

Financial support from the Australian Renewable Energy Agency (ARENA) is gratefully acknowledged.

REFERENCES

[1] C.S. Turchi, Z. Ma, T.W. Neises, and M.J. Wagner, "Thermodynamic Study of Advanced Supercritical Carbon Dioxide Power Cycles for Concentrating Solar Power Systems," *J. Solar Energy Engineering*, 135 (2013) 041007-1.

[2] J. Pasch, T. Conboy, D. Fleming, and G. Rochau, Supercritical CO_2 Recompression Brayton Cycle: Completed Assembly Description, SANDIA REPORT, SAND2012-9546, 40p, October 2012.

[3] V. Dostal, PhD Thesis – *A Supercritical Carbon Dioxide Cycle for Next Generation Nuclear Reactors,* Massachusetts Institute of Technology, January 2004.

[4] C.T. Fujii and R.A. Meussner. Carburisation of Fe-Cr Alloys during Oxidation in Dry Carbon Dioxide, J. Electrochem. Soc., 114 (1967) pp 435-441.

[5] F.S. Pettit, J.A. Goebel, and G.W. Goward, *Corros. Sci.*, 9 (1969) 903-913.

[6] F. Rouillard, G. Moine, M. Tabarant, and J.C. Ruiz. Corrosion of 9Cr Steel in CO_2 at Intermediate Temperature II: Mechanism of Carburisation, *Oxid. Met*., 77 (2012) pp 57-70.

[7] F. Rouillard, G. Moine, L. Martinelli, and J.C. Ruiz. Corrosion of 9Cr Steel in CO_2 at Intermediate Temperature I: Mechanism of Void-Induced Duplex Oxide Formation, *Oxid. Met*., 77 (2012) pp 27-55.

[8] H.E. McCoy. Type 304 Stainless Steel versus Flowing CO_2 at Atmospheric Pressure, *Corrosion*, 21 (1965) pp 84-89.

[9] P. Promdirek, G. Lothongkum, S. Chandra-Ambhorn, Y. Wouters, and A. Galerie. Oxidation Kinetics of AISI 441 Ferritic Stainless Steel at High Temperatures in CO_2 Atmosphere, *Oxid. Met*., 81 (2014) pp 315-329.

[10] S.B. Newcomb, W.M. Stobbs, and E. Metcalfe. A Microstructural Study of the Oxidation of Fe-Ni-Cr Alloys I. Protective Oxide Growth, *Phil. Trans. Royal Soc. A*, 319 (1986) pp 191-218.

[11] W.M. Stobbs, S.B. Newcomb, and E. Metcalfe, A Microstructural Study of the Oxidation of Fe-Ni-Cr Alloys II. Non-Protective Oxide Growth, *Phil. Trans. Royal Soc. A*, 319 (1986) pp 219-247.
[12] S. Bouhieda, F. Rouillard, and K. Wolski, Influence of CO_2 Purity on the Oxidation of a 12Cr Ferritic-Martensitic Steel at 550^{o}C and Importance of the Initial Stage, Mater. High Temp., 29 (2012) 151.
[13] J. Pirón-Abellán, T. Olszewski, H.J. Penkalla, G.H. Meier, L. Shingheiser, and W.J. Quadakkers, Scale Formation Mechanisms of Martensitic Steels in High CO_2/H_2O-Containing Gases Simulating Oxyfuel Environments, Mater. High Temp., 26 (2009) pp 63-72.
[14] C. Gleave, J.M. Calvert, D.G. Lee, and P.C. Rowlands, A Study of the Mechanism of Corrosion of Some Ferritic Steels in High-Pressure Carbon Dioxide with the Aid of Oxygen-18 as a Tracer. I: Low-Silicon Mild Steel, Proc. Roy. Soc. London A, 379 (1982) pp 409-427.
[15] L. Tan, M. Anderson, D. Taylor, and T.R. Allen, Corrosion of Austenitic and Ferritic-Martensitic Steels Exposed to Supercritical Carbon Dioxide, Corros. Sci., 53 (2011) pp 3273-3280.
[16] G. Cao, V. Firouzdor, K. Shridharan, M. Anderson, and T.R. Allen, Corrosion of Austenitic Alloys in High Temperature Supercritical Carbon Dioxide, Corros. Sci., 60 (2012) pp 246-255.
[17] V. Firouzdor, K. Shridharan, G. Cao, M. Anderson, and TY.R. Allen, Corrosion of a Stainless Steel and Nickel-based Alloys in High Temperature Supercritical Carbon Dioxide Environment, *Corros. Sci.*, 69 (2013) pp. 281-291.
[18] T. Gheno, D. Monceau, J. Zhang, and D. Young, Carburisation of Ferritic Fe-Cr Alloys by Low Carbon Activity Gases, *Corros. Sci*., 53 (2011) pp 2767-2777.
[19] C. Wagner, Theoretical Analysis of the Diffusion Processes Determining the Oxidation Rate of Alloys, *J. Electrochem. Soc*., 99 (1952) pp 369-380.
[20] I. Wolf and H.J. Grabke, A Study on The Solubility and Distribution of Carbon in Oxides, Solid State Communications, 54 (1985) pp 5-10.
[21] D. Young, T.D. Nguyen, P. Felter, J. Zhang, and J. Cairney, Penetration of Protective Chromia Scales by Carbon, Scripta Mater., 77 (2014) pp 29-32.
[22] X.G. Zheng and D.J. Young, High-Temperature Corrosion of Cr2O3 Forming Alloys in CO-CO_2-N_2 Atmospheres, Oxid. Met., 42 (1994) pp 163-190.
[23] S. Bouhieda, F. Rouillard, V. Barnier, and K. Wolski, Selective Oxidation of Chromium by O_2 Impurities in CO_2 During Initial Stages of Oxidation, Oxid. Met., 80 (2013) pp 493-503.
[24] D.J. Young, *High Temperature Oxidation and Corrosion of Metals*, 2nd ed., Elsevier (Amsterdam, 2016).
[25] R.I. Olivares, P. Marvig, D.J. Young and W. Stein, Alloys SS316 and Hastelloy-C276 in Supercritical CO_2 at High Temperature, *Oxid. Met.*, 84 (2015) pp 585-606.
[26] C. Wagner, Z. Elektrochem., 63 (1959) 772.
[27] O. Kubaschewski, C. B. Alcock and P.J. Spencer, *Materials Thermochemistry*, 6th ed., Pergamon Press (1993).
[28] T. Wada, H. Wada, J. F. Elliott and J. Chipman, *Met. Trans.*, 2A (1971) 2199.
[29] S. K. Bose and H. J. Grabke, *Z. Metallk.*, 69 (1978) 8.
[30] J. Zhang and D.J. Young, *Corros. Sci*., 56 (2012) pp 184-193.
[31] A. La Fontaine, B. Gault, A. Breen, L. Stephenson, A.V. Ceguerra, L. Yang, T.D. Nguyen, J. Zhang, D.J. Young, J.M. Cairney, Interpreting atom probe data from chromium oxide scales, ***Ultramicroscopy***,159 (2015) 354-359.